

A Rare Millisecond Pulsar with Cross-Pole Emission: Single-Pulse Insights from PSR J1857+0943

SHI-JUN DANG ,^{1, 2} JI-GUANG LU,^{1, 3, 4} PENG JIANG,^{1, 3, 4} YU-LAN LIU ,^{1, 3, 4} JIN-TAO XIE,⁵
 HABTAMU MENBERU TEDILA ,^{3, 4, 6} FEI-FEI KOU ,⁷ JIAN-PING YUAN,⁷ ZHI-GANG WEN,⁷ SHUANG-QIANG WANG ,⁷
 LUN-HUA SHANG,² ZU-RONG ZHOU ,⁸ WEN-MING YAN,⁷ QI-JUN ZHI,^{9, 2} AND NA WANG⁷

¹Guizhou Radio Astronomical Observatory, Guizhou University, Guiyang 550001, People's Republic of China

²School of Physics and Electronic Science, Guizhou Normal University, Guiyang 550001, People's Republic of China

³CAS Key Laboratory of FAST, NAOC, Chinese Academy of Sciences, Beijing 100101, People's Republic of China

⁴National Astronomical Observatories, Chinese Academy of Sciences, Beijing 100101, People's Republic of China

⁵School of Computer Science and Engineering, Sichuan University of Science and Engineering, Yibin 644000, China

⁶Arba Minch University, Arba Minch 21, Ethiopia

⁷XinJiang Astronomical Observatory, CAS, Urumqi, Xinjiang 830011, People's Republic of China

⁸National Time Service Center, Chinese Academy of Sciences, Xi'an 710600, China

⁹College of Physics, Guizhou University, Guiyang, Guizhou 550025, People's Republic of China

ABSTRACT

Studies of subpulse variability in millisecond pulsars (MSPs) offer important constraints on their emission physics. Using the high sensitivity of FAST, we present the first identification of distinct single pulse fluctuation behaviour in PSR J1857+0943. We find that the third component(MP_C3) of the main pulse may originate from a different region than the other two main-pulse components and may instead share a common origin with the interpulse. This conclusion is supported by four observational evidence as follows: First, the LRCCF shows a clear anticorrelation between MP_C3 and the interpulse. Second, the single-pulse polarization at the main-pulse longitude reveals obvious component mixing. Third, the modulation period of the interpulse components is roughly twice that of MP_C3. Fourth, the reduced modulation index in MP_C3 suggests possible mixing of emission from different regions. The interpretation in this letter contrasts with the usual assumption that the main pulse and interpulse originate from opposite magnetic poles. Hence, PSR J1857+0943 provides a rare laboratory for probing component-dependent plasma behaviour in an MSP magnetosphere. Our results offer direct evidence that the main pulse can include emission associated with more than one magnetic pole and highlight the importance of single-pulse diagnostics for understanding the geometry and dynamics of pulsars with interpulse emission. In addition, we analyse the jitter properties of this pulsar and measure a one-hour jitter of $\sigma_{J,1h} = 78 \pm 3$ ns at 1.25 GHz, consistent with previous studies.

Keywords: pulsars: general – pulsars: individual: PSR J1857+0943

1. INTRODUCTION

Millisecond pulsars (MSPs) are known for their exceptionally stable periods, making them the most precise timekeepers in the universe. Due to their exceptional rotational stability and high spin frequencies, millisecond pulsars (MSPs) provide unmatched precision in pulsar

timing. The high timing precision of MSPs makes them invaluable probes for studying the dense matter physics of neutron stars (NSs)(Özel & Freire 2016; Deng et al. 2020), testing gravitational theories(Ransom et al. 2014; Zhu et al. 2015; Wu et al. 2023), detecting the nHz gravitational wave background (eg. Taylor 1992; Kerr et al. 2020; Chalumeau et al. 2022; Xu et al. 2023; Agazie et al. 2023; EPTA Collaboration et al. 2023). Additionally, MSPs have also been used to detect the structures and turbulence of the interstellar medium (Coles et al. 2015; Liu et al. 2023; Zhang et al. 2023), the magnetic

lujig@nao.cas.cn(J. G. Lu)

pjiang@nao.cas.cn(P. Jiang)

field structure in the Galaxy (Han et al. 2018), and so on (Hobbs 2013).

The integrated pulse profile of a pulsar is highly stable, similar to a human fingerprint, but the shape of the individual pulses that construct the integrated profile can vary significantly. The emission variation in individual pulses usually include model changing(eg. Drake & Craft 1968), nulling(eg. Backer 1970), subpulse drifting(eg. Drake & Craft 1968), periodic amplitude modulation(eg. Basu et al. 2025), giant pulseKuzmin (eg. 2007), and so on. The individual pulse emission variation phenomena have been widely studied in canonical pulsars (eg. Basu et al. 2019, 2020; Song et al. 2023; Xu et al. 2024). However, only few MSPs have shown evidence of mode changing (eg. Mahajan et al. 2018; Wang et al. 2020, 2021; Miles et al. 2022) or sub-pulse drifting (Edwards & Stappers 2002; Liu et al. 2016; Miao et al. 2023). MSPs are rarely detected with single pulse variations due to their short rotation periods and weak radiation. Therefore, studying the single pulse variations of MSPs requires telescopes with high sensitivity and high time resolution. FAST will provide a great opportunity to conduct this research(Wang et al. 2024; Xu et al. 2025b).

PSR J1857+0943 was discovered by the Arecibo radio telescope in 1986. It has a rotation period of 5.362 milliseconds, a white dwarf companion, and orbits a nearly circular orbit with a period of approximately 12.3 days(Segelstein et al. 1986; van Kerkwijk et al. 2000). The previous studies have not detected its single pulse variation behavior. In this paper, we have analyzed the single pulse modulation and polarization of PSR J1857+0943 using the high-sensitivity FAST Observation. The details of observations and data processing are presented in Section 2, and the results are presented in Section 3. The conclusion and discussion of the study are presented in Section 4.

2. OBSERVATIONS AND DATA REDUCTION

The Five-hundred-meter Aperture Spherical Radio Telescope(FAST) is located in Guizhou province in China. FAST is the most sensitive single-aperture radio telescope in the world, it has an effective illumination aperture of 300 meters during normal operation (Nan et al. 2011; Jiang et al. 2019). In this paper, we use the data collected by the center beam of the 19-beam receiver with a covering bandwidth range from 1.05–1.45 GHz and recorded by a digital backend based on Reconfigurable Open-architecture Computing Hardware—version2 (ROACH2) (Li et al. 2018; Jiang et al. 2019, 2020). The data was recorded in search mode and with the data format as PSRFITS (Hotan

et al. 2004). We chose to record 4 polarizations and 8-bit samples. The sampling intervals is $8 \mu\text{s}$, frequency channels is 1024, and the observation duration is 1726s. To calibrate the data, our observation contains a stable noise signal injected by a single diode.

After obtaining the data, we first processed the data using DSPSR software package (van Straten & Bailes 2011) and eliminated the dispersion delays in the inter-channel using the $-K$ option. Here, the pulsar ephemeris was obtained from the Australia Telescope National Facility(ATNF) pulsar catalogue (PSRCAT V-2.51 (Manchester et al. 2005) ¹). We use 512 phase bins to achieve high time resolution in the pulse profile. Secondly, the narrow-band radio frequency interference (RFI) and 5% of the band-edges were removed by using the PAZ package provided by the PSRCHIVE software (Hotan et al. 2004). Finally, the polarization was calibrated by using the PAC package of PSRCHIVE software with the noise signal. Rotation measure (RM) was measured by using the RMFIT package of PSRCHIVE software. The resulting RM is $33.32 \pm 1.52 \text{ rad m}^{-2}$. The contribution from the Earth’s ionosphere was estimated using IONFR (Sotomayor-Beltran et al. 2013), giving $4.01 \pm 0.26 \text{ rad m}^{-2}$. After correcting for this ionospheric contribution, the rotation measure originating from the interstellar medium is $29.31 \pm 1.54 \text{ rad m}^{-2}$. This interstellar RM value was subsequently adopted for all polarization calibration and position angle (PA) corrections applied in our analysis.

3. RESULTS

3.1. Periodic emission variation

In total, 322,046 individual pulses from PSR 1857+0943 were analyzed. In order to analyze the individual pulse properties of pulsars, it is customary to reformat the de-dispersed one-dimensional time series into a two-dimensional pulse stack, mapping pulse longitude as a function of pulse number. The upper panel of Figure 1 presents the pulse stack for the first 200 single pulses, where evident intensity modulation can be seen from pulse to pulse. By vertically integrating the pulse stack over full dataset, we obtained the integrated pulse profile, as shown in the middle panel of Figure 1. The profile clearly reveals a prominent main pulse (MP) and a distinct interpulse (IP). Each of these two features is resolved into three separable components in phase(MP_C1, MP_C2, MP_C3, IP_C1, IP_C2, and IP_C3).

3.1.1. The modulation index

¹ <http://www.atnf.csiro.au/research/pulsar/psrcat/>

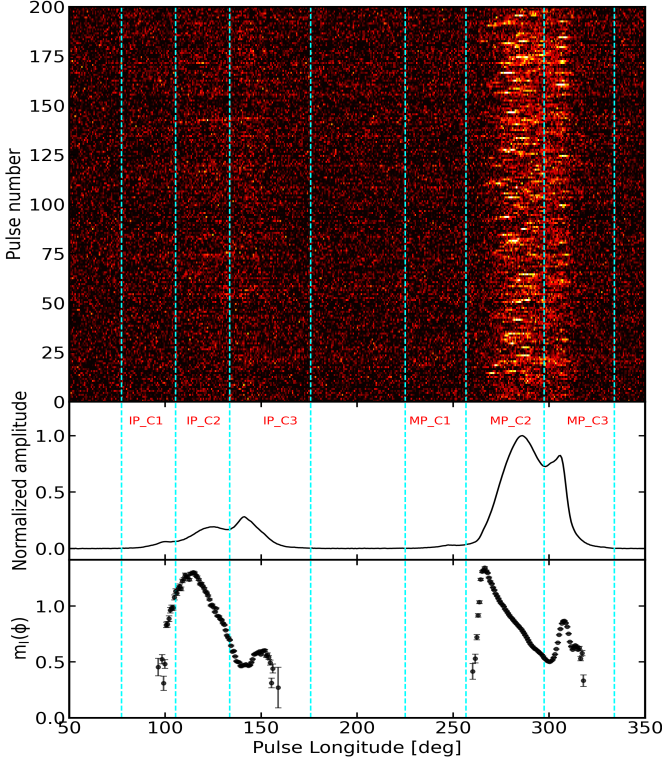


Figure 1. Single-pulse sequence and integrated pulse profile for PSR J1857+0943. The upper panel shows the first 200 pulses in grayscale. The middle panel displays the integrated profile from all 322,046 pulses, with the main pulse (MP) and interpulse (IP) each resolved into three components. The lower panel shows the phase-resolved modulation index computed from the full set of 322,046 pulses. The cyan dashed lines mark the boundaries of the different profile components.

To quantitatively characterize the observed pulse-to-pulse intensity variation, we calculated the longitude-resolved modulation index m , defined as

$$m = \frac{\sigma_{\text{pulse}}}{\mu_{\text{pulse}}} \quad (1)$$

where σ_{pulse} and μ_{pulse} are the intrinsic pulse standard deviation and mean pulse intensity at each longitude bin, after correcting for the contribution of the radiometer noise from the off-pulse region. The calculation of $m_I(\phi)$ in this work follows the standard formulation, with corrections applied for the contribution of radiometer noise estimated from the off-pulse region. In our analysis, the baseline level of each pulse was determined using a single off-pulse window consisting of N phase bins. The statistical effect of this baseline subtraction introduces a small bias in the measured variances, which is explicitly corrected. The final expression for the mod-

ulation index is given by

$$m = \frac{\sigma_{\text{pulse}}}{\mu_{\text{pulse}}} = \frac{\sqrt{\sigma_{\text{on}}^2 - \frac{N+1}{N-1}\sigma_1^2}}{\mu_{\text{on}}}, \quad (2)$$

where σ_{on} and μ_{on} denote the standard deviation and mean of the on-pulse region after baseline subtraction, σ_1 represents the standard deviation of the off-pulse region after baseline subtraction, and $\frac{N+1}{N-1}$ is the correction factor accounting for the statistical coupling introduced by the finite off-pulse window. A detailed derivation of this correction is presented in A

The phase-resolved modulation index map shows in the bottom panel of Figure 1, it reveals clear trends in variability across the pulse profile. For the IP region, the modulation index increases from the IP_C1 region, reaching a peak of $m = 1.302 \pm 0.010$ at a phase of $\sim 111.1^\circ$ at the leading edge of IP_C2. It then decreases to a minimum of $m = 0.312 \pm 0.043$ at $\sim 144.1^\circ$ within IP_C3, followed by a small rebound to a secondary peak of $m = 0.441 \pm 0.041$ at $\sim 144.8^\circ$. For the MP region, the modulation index rises from the leading edge, attaining its global maximum of $m = 1.344 \pm 0.007$ at $\sim 224.3^\circ$ at the leading edge of MP_C2. After this peak, it declines to a minimum of $m = 0.612 \pm 0.001$ at the trailing edge of MP_C2 around $\sim 297.4^\circ$. In the MP_C3 region, the modulation index rises again, reaching a secondary peak of $m = 0.868 \pm 0.002$ at its center around $\sim 328.4^\circ$, before decreasing towards the end of the pulse profile. It is worth noting that mixing between adjacent profile components can reduce the apparent modulation index. Such mixing effects may therefore contribute to the gradual decrease in m observed across several parts of both the IP and MP regions.

3.1.2. LRFS

To investigate the subpulse modulation behavior, we computed the longitude-resolved fluctuation spectrum (LRFS) following the standard fluctuation analysis technique (Backer 1970; Edwards & Stappers 2002). To do that, the single-pulse data were first arranged into a two-dimensional array, where each row corresponds to one pulse and each column represents a longitude bin within the pulse window. The pulse sequence was then divided into contiguous blocks of 512 pulses. For each block, only the on-pulse longitude bins were selected. To eliminate the DC component of the fluctuation spectrum, the mean intensity at each pulse longitude was subtracted. A Fast Fourier Transform (FFT) was then performed along the pulse number axis for every longitude bin, converting temporal intensity variations into modulation power as a function of fluctuation frequency. The final LRFS was obtained by averaging the power

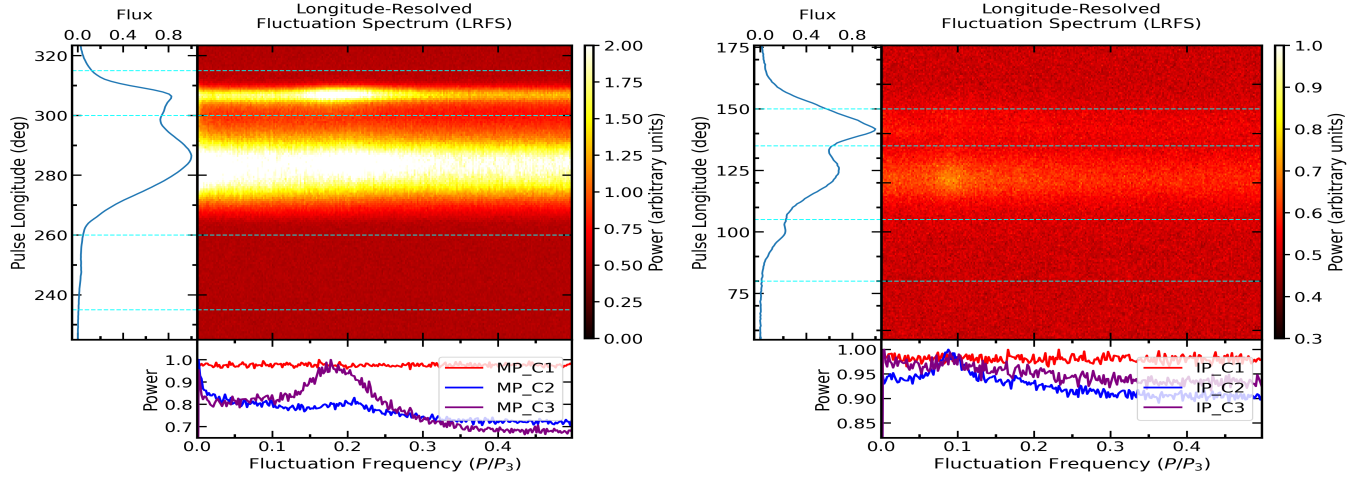


Figure 2. Longitude-resolved fluctuation power spectra for the main pulse (left) and interpulse (right) of PSR J1857+0943. The main panel in each plot shows the LRFS, the left panel displays the integrated pulse profile, and the bottom panel shows the total power spectrum of P/P_3 . The total power spectrum in the bottom panel is obtained by vertically integrating the LRFS within the region enclosed by the cyan dashed lines. The red, blue, and purple curves represent the total P/P_3 power for the components MP_C1, MP_C2, and MP_C3, respectively.

spectra over all data blocks. Figure 2 shows the resulting LRFS for the MP and IP of PSR J1857+0943. The vertical axis represents the pulse longitude, the horizontal axis corresponds to the modulation frequency, and the spectral intensity indicates the modulation power. The peak frequency in the LRFS reveals the subpulse repetition periodicity (P_3) at a given pulse longitude, expressed as $(P/P_3$, in units of cycles per rotation period, cpp), where P denotes the rotation period. In each panel, the main map shows the LRFS, the left subpanel displays the integrated pulse profile, and the bottom subpanel presents the total fluctuation power spectrum as a function of P_1/P_3 , obtained by vertically integrating the LRFS between the cyan dashed lines. The total power spectra from the LRFS reveals distinct modulation features across the emission components for PSR J1857+0943. For the main pulse, no significant peak is detected for MP_C1 (red), a weak peak is present for MP_C2 (blue), and a prominent peak is seen for MP_C3 (purple). For the interpulse (IP), IP_C1 (red) shows no detectable peak, IP_C2 (blue) exhibits a prominent peak, while IP_C3 (purple) shows a weaker one. The peaks for MP_C2 and MP_C3 correspond to a modulation frequency of $P_3 \approx 0.19$ cpp, whereas those for IP_C2 and IP_C3 correspond to $P_3 \approx 0.09$ cpp. The absence of significant peaks in MP_C1 and IP_C1 suggests a lack of stable, periodic subpulse modulation in these regions.

3.1.3. 2DFS

Although the LRFS is a powerful tool for determining the time-averaged properties of periodic subpulse modulations, it remains uncertain whether the

detected modulation arises from intensity or phase variations. To further investigate this ambiguity, we computed two-dimensional fluctuation spectra (2DFS) for each of the six resolved profile components of PSR J1857+0943 (MP_C1, MP_C2, MP_C3, IP_C1, IP_C2, and IP_C3), following the procedure of [Edwards & Stappers \(2002\)](#). The pulse sequence was divided into contiguous blocks of 512 pulses, and a two-dimensional discrete Fourier transform (DFT) was applied to the on-pulse window of each block. The spectra from all blocks were averaged to obtain the final 2DFS (Figure 3), with the vertical axis representing the subpulse modulation frequency (P_3 , in cpp) and the horizontal axis corresponding to the longitudinal pattern repetition frequency (P_2 , in cpp). For each component, the P_3 and P_2 values were derived by performing Gaussian fits to the spectral data points near the respective peaks, with uncertainties taken directly from the fit parameters. No significant P_3 features were detected in MP_C1 and IP_C1. In contrast, both MP_C2 and MP_C3 show similar vertical modulation frequencies, with P_3 values of 0.195 ± 0.005 cpp and 0.182 ± 0.003 cpp, respectively, consistent within uncertainties and corresponding to a modulation period of approximately $P_3 \sim 5 P$. Likewise, IP_C2 and IP_C3 exhibit comparable P_3 values of 0.090 ± 0.002 cpp and 0.091 ± 0.009 cpp, corresponding to a period of $P_3 \sim 11 P$. Thus, the modulation period in IP_C2 and IP_C3 is approximately twice that observed in MP_C2 and MP_C3.

In all six components, the measured P peaks are consistent with zero within their uncertainties, except for the MP_C2 component, which exhibits a small but

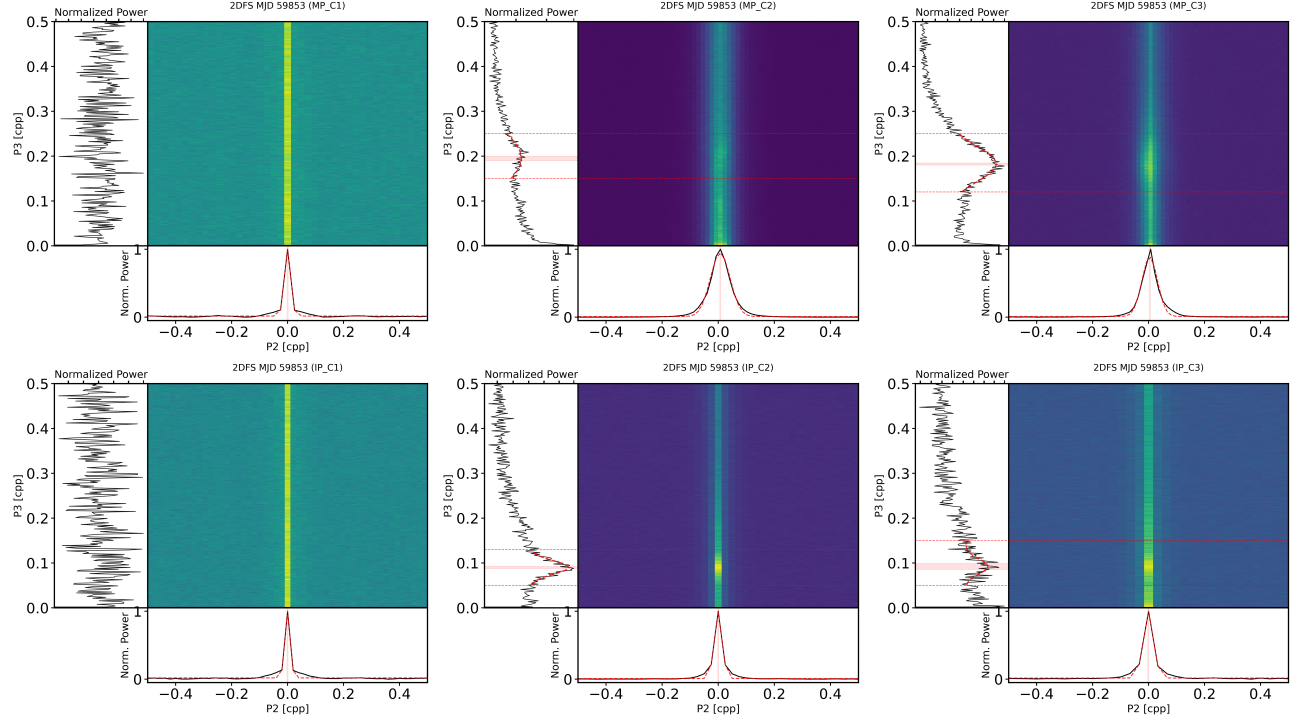


Figure 3. Two-dimensional fluctuation power spectra (2DFS) for the six resolved profile components of PSR J1857+0943. Each main panel presents the full spectrum as a color-coded plot, with the vertical axis representing the subpulse repetition frequency (P/P_3 , in cycles per period, cpp) and the horizontal axis representing the longitudinal spacing repetition rate (P/P_2 , in cpp). The left-hand side sub-panel shows the vertically integrated total P_3 power, where the horizontal red dashed line indicates the Gaussian fit to the spectral feature, and the horizontal red band marks the corresponding P_3 3σ uncertainty range from the fit. Similarly, the bottom sub-panel displays the horizontally integrated total P_2 power, in which the vertical red dashed line represents the Gaussian fit to the P_2 feature, and the vertical red band denotes the P_2 3σ uncertainty range.

measurable offset of $P_2 = 0.007 \pm 0.002$ cpp, corresponding to a longitude separation of approximately $2.52^\circ \pm 0.72^\circ$. For all other components, the P_2 peak remains indistinguishable from zero. This indicates that MP_C2 exhibits a signature compatible with relatively rapid diffused subpulse drifting, whereas all other components show no measurable phase gradient. Consequently, the modulation in those regions is dominated by quasi-periodic amplitude variations rather than systematic drifting behavior.

3.1.4. LRCCF

As an additional diagnostic of pulse-to-pulse correlations beyond the LRFS and 2DFS analysis, we computed the Longitude-Resolved Cross-Correlation Function (LRCCF), which quantifies the covariance between every pair of pulse longitudes as a function of pulse number lag. This technique is sensitive to both systematic subpulse drifting, manifested as inclined correlation ridges, and purely amplitude-modulated fluctuations, which typically yield vertical and lag-independent correlation features.

Figure 4 presents the LRCCF map evaluated at lag = 1. The most prominent feature is a strong, positively

sloped correlation ridge associated with MP_C2. Its slight offset from the diagonal further demonstrates the presence of longitude-dependent phase evolution. This coherent structure is fully consistent with the rapid drifting behavior inferred from the 2DFS analysis. In contrast, MP_C3 show nearly vertical correlation patches without discernible slope, suggesting that the variability there is dominated by correlated emission from two distinct sub-beam or emission regions rather than by systematic phase drift. In addition to the positive correlations, the LRCCF map also reveals distinct regions of anti-correlation, particularly between MP_C3 and IP_C2. This behavior suggests that intensity enhancements in MP_C3 tend to coincide with reduced emission in IP_C2, hinting at a possible coupling mechanism between emission regions separated in phase. The LRCCF results reinforce the conclusion that MP_C2 exhibits the most significant drifting behavior within the profile, while the remaining components mostly lack measurable phase gradients and instead display stochastic or amplitude-modulated variability.

3.2. The averaged polarization profile

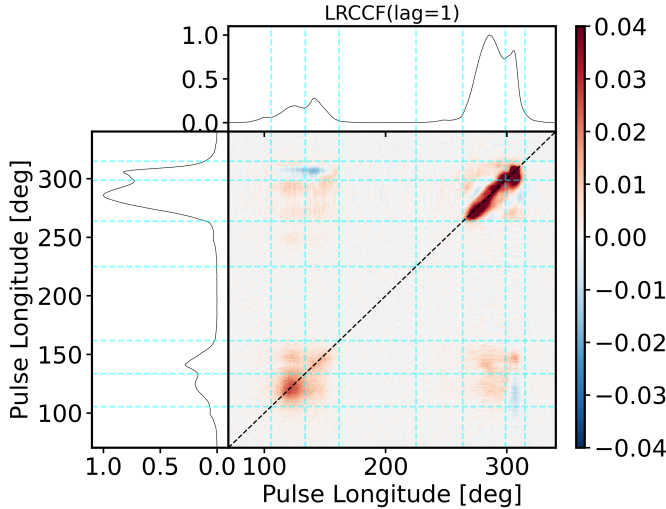


Figure 4. Longitude-resolved cross-correlation map with itself at a delay of $1P$ calculated over the entire 322,046 single-pulses. The main panel shows the correlation between different longitudes as marked by the profile in both the top and left panels. The cyan dashed lines mark the boundaries of the different profile components.

The mean pulse profile and polarization properties of a pulsar are important for understanding the pulse emission mechanism, the beaming of pulsar radiation, and the emission geometry. The polarization profile and the swing of linear polarization position angle (PA) of PSR J1857+0943 at 1.25 GHz are shown in Figure 5. We detect only weak bridge emission in our integrated pulse profile (around a pulse longitude of 180 to 250 degrees), and its significance is lower than the clearer structure reported in the literature (Xu et al. 2025a), likely due to the relatively low signal-to-noise ratio of our observation. To calculate the fractional linear polarization ($\langle L \rangle / I$), the fractional net circular polarization ($\langle V \rangle / I$), and the fractional absolute circular polarization ($\langle |V| \rangle / I$) of the profile, all polarization parameters were derived from the average polarization profile. The on-pulse window was defined as the portion of the pulse profile where the total intensity exceeds three times the baseline rms noise. The measured polarization fractions are $\langle L \rangle / I = 14.3\%$, $\langle V \rangle / I = -0.6\%$, and $\langle |V| \rangle / I = 4.7\%$, which are in general consistent with the values of 14.2%, -0.1%, and 4.3% reported in (Xu et al. 2025a). Notably, in the single-pulse PPA distribution of the main pulse, we identify two distinct structures near pulse longitudes of 280° and 310° , corresponding to the MP_C2 and MP_C3 regions, respectively. These features deviate significantly from the average-pulse PPA curve, and they are also inconsistent with the polarization-angle bifurcations described by Dyks (2017). These observations suggest that the emission at

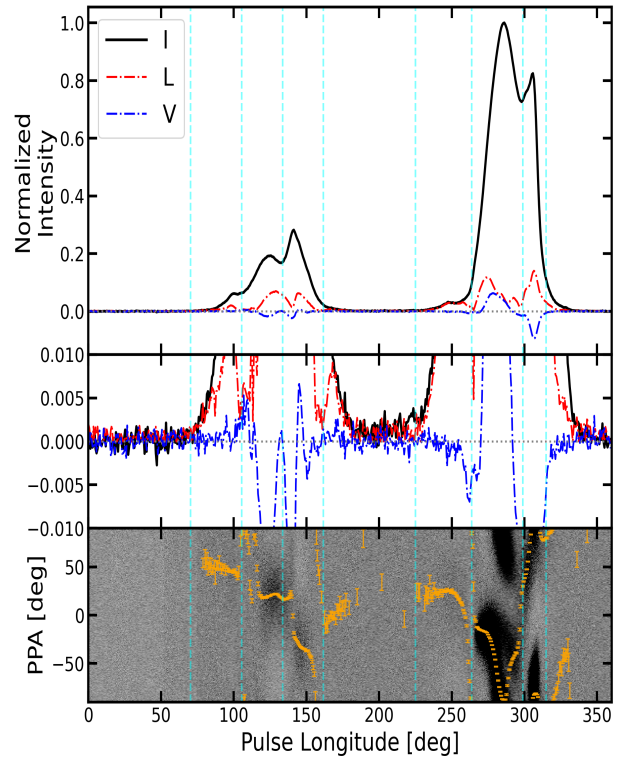


Figure 5. Polarized pulse profile for PSR J1857+0943. The top panel shows the polarized profile, where the black solid line, the red dashed line, and the blue dashed line represent the total intensity (I), linear polarization (L), and circular polarization (V), respectively. The middle panel is an expanded plot showing low-level details of the polarization profiles, with the horizontal grey dashed line indicating the baseline (0). The bottom panel shows the PPA of the average profile (yellow) and the single-pulse PPA distribution (grey scale). The cyan dashed lines mark the boundaries of the different profile components.

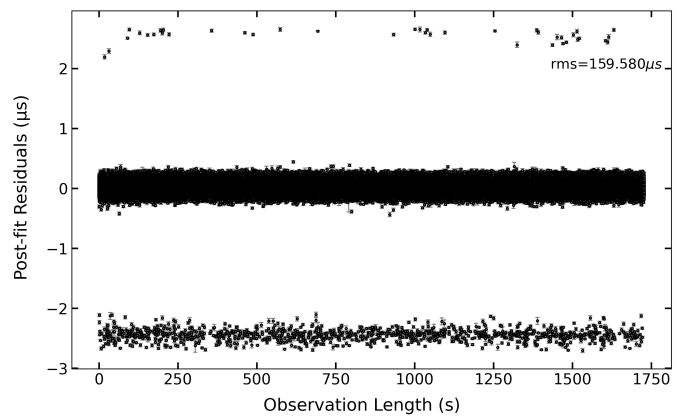


Figure 6. Post-fit timing residuals of PSR J1857+0943.

MP_C3 may originate from independent emission re-

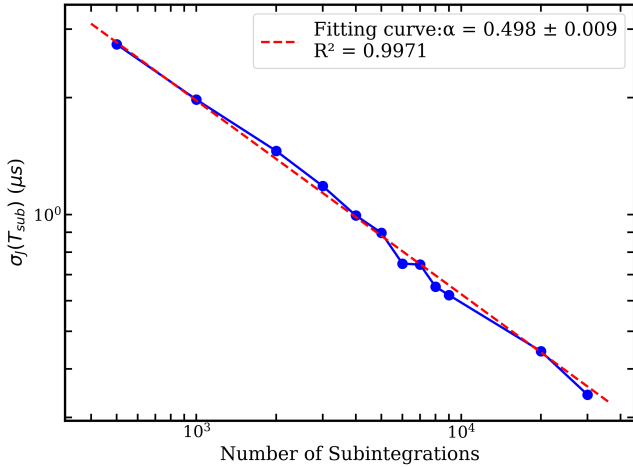


Figure 7. Evolution of jitter noise characteristics as a function of the number of integrated pulses (N_p) in PSR J1857+0943. The blue dot presents the $\sigma_J(N_p)$, and the dashed red curve represents the best-fit jitter noise scaling relation, with a power-law index of -0.498 ± 0.009 .

gions, although the possibilities of propagation effects and mode mixing cannot be fully ruled out.

3.3. Single Pulse Timing and Jitter

Pulse-to-pulse morphology variations, commonly referred to as jitter, have been extensively studied in pulsars employed for pulsar timing arrays (PTAs), as they impose a fundamental limit on the achievable timing precision(Oslowski et al. 2011; Liu et al. 2012; Shannon et al. 2014; Lam et al. 2019; Parthasarathy et al. 2021; Wang et al. 2024). On short timescales, the timing residuals of pulsars are primarily dominated by radiometer noise, which can be reasonably represented by the uncertainties in the measured times of arrival (ToAs). Over longer timescales, variability in individual pulses can introduce jitter noise, potentially degrading the precision of highly sensitive observations. The effect of jitter may be mitigated by selectively including an optimized subset of single pulses in the timing analysis(Wang et al. 2020).

In our single-pulse timing analysis of PSR J1857+0943, we identified two distinct emission components corresponding to the main pulse and the interpulse. When all single pulses were included without distinguishing between these components, the post-fit timing residuals exhibited two clearly separated clusters in phase space (see Figure 6). The root-mean-square (rms) of the residuals for the total sample was measured to be $159.58 \mu\text{s}$. However, when the integration length was increased to include more than ~ 1000 pulse periods per subintegration, this separation disappeared in

PSR J1857+0943. The merging of the residual distributions under longer averaging times suggests that the pulse-to-pulse mode variations are effectively averaged out, leading to a single stable mean profile.

We quantified the pulse jitter noise following the formalism of Parthasarathy et al. (2021) and Wang et al. (2024). Using frequency-averaged timing analysis, the observation was divided into contiguous blocks with varying numbers of averaged pulses T_{sub} , from single pulses to long subintegrations. For each T_{sub} , we first generated ToAs corresponding to a range of increasing sub-integration lengths, and obtained timing residuals by subtracting a timing model based on the `psrcat` ephemeris. In this procedure, only the spin frequency was fitted, while all other timing parameters were held fixed, ensuring that the resulting residuals retained the short-timescale stochastic contributions intrinsic to the pulsar. The covariance matrix of these residuals therefore contains contributions from both radiometer noise and pulse-to-pulse jitter. The jitter noise $\sigma_J(T_{\text{sub}})$ was then obtained as the follow relation:

$$\sigma_{\text{ToA}}^2(T_{\text{sub}}) = \sigma_{\text{S/N}}^2(T_{\text{sub}}) + \sigma_J^2(T_{\text{sub}}) \quad (3)$$

where $\sigma_{\text{ToA}}^2(T_{\text{sub}})$ represents the observed covariance in the residuals, $\sigma_{\text{S/N}}^2(T_{\text{sub}})$ is the contribution due to radiometer noise from the receiver system, and $\sigma_J^2(T_{\text{sub}})$ represents the contribution from pulse jitter.

To estimate $\sigma_{\text{S/N}}^2(T_{\text{sub}})$, we performed simulations using TEMPO2 plugins following the same method used in (Parthasarathy et al. 2021). Ideal ToAs were first generated using the `formIdeal` plugin based on the adopted timing model. Gaussian noise consistent with the radiometer-limited ToA uncertainties was then added using the `addGaussian` and `createRealisation` plugins. To robustly estimate the radiometer-noise covariance, 1000 realisations were generated for every integration length. The mean covariance matrix from these simulations, which contains only the radiometer contribution and is diagonal by construction, was subtracted from the covariance matrix of the real FAST residuals. The resulting set of jitter covariance matrices allowed us to measure the evolution of the jitter noise amplitude as a function of sub-integration time.

The measured $\sigma_J(T_{\text{sub}})$ values span from $2.74 \mu\text{s}$ at $T_{\text{sub}} = 500$ to $0.34 \mu\text{s}$ at $T_{\text{sub}} = 30000$. Figure 7 presents evolution of $\sigma_J(T_{\text{sub}})$ as a function of N_p in PSR J1857+0943. A power-law fit of the form

$$\sigma_J(T_{\text{sub}}) = AT_{\text{sub}}^\alpha \quad (4)$$

was applied, yielding $\alpha = -0.498 \pm 0.009$, consistent with the theoretical expectation of $\alpha = -0.5$ for uncorrelated pulse-to-pulse shape variations(e.g., Cordes

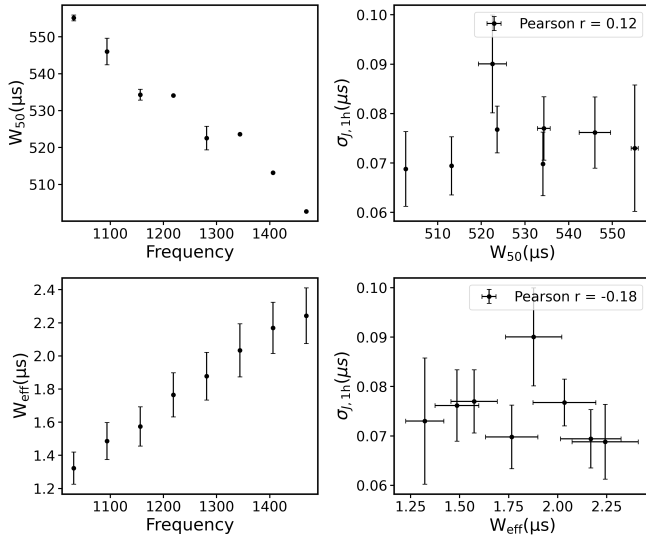


Figure 8. Frequency dependence and jitter correlation of the pulse width parameters for PSR J1857+0943. Top left: Frequency evolution of the W_{50} . Top right: $\sigma_{J,1h}$ versus W_{50} . Bottom left: Frequency evolution of W_{eff} . Bottom right: $\sigma_{J,1h}$ versus W_{eff} . Pearson correlation coefficients are indicated in the scatter plots.

& Shannon 2010; Shannon et al. 2014; Liu et al. 2012). To allow a direct comparison with previous studies, we fitted the evolution of jitter with integration time based on the theoretically expected ($T_{\text{sub}}^{-1/2}$) scaling, and extrapolated to a one-hour integration, obtaining ($\sigma_{J,1h} = 78 \pm 3$ ns), which is in good agreement with the previously reported value of 60 ± 25 ns by Palliyaguru et al. (2023).

We also investigate the correlation between the $\sigma_{J,1h}$, and different estimates of the pulse width, including the pulse widths at 50 per cent (W_{50}) and the effective pulse width (W_{eff}), measured from the integrated profiles at different observing frequencies (Figure 8). We estimate the W_{eff} following the definition in Downs & Reichley (1983) and Cordes & Shannon (2010). We find that W_{50} systematically decreases with increasing frequency, consistent with the expectations from radius-to-frequency mapping. In contrast, W_{eff} shows an increasing trend with frequency, indicating that the pulse profile becomes progressively sharper at higher frequencies. There is no significant correlation is found between $\sigma_{J,1h}$ and either W_{50} or W_{eff} .

4. CONCLUSION AND DISCUSSION

We have investigated the single-pulse properties of PSR J1857+0943 using a 1726s FAST observation comprising 322,046 individual rotations. The 2DFS analysis reveals clear, component-dependent periodic emission variations. In MP_C2 we detect weak system-

atic subpulse drifting, with measured values of $P_2 = 0.007 \pm 0.002 \text{ cpp}$ and $P_3 = 0.195 \pm 0.005 \text{ cpp}$. In contrast, MP_C3 exhibits only periodic amplitude modulation, with $P_3 = 0.182 \pm 0.003 \text{ cpp}$ and no evidence of systematic phase drift. Periodic modulation is also present in the interpulse, where we measure $P_3 = 0.090 \pm 0.002 \text{ cpp}$ in IP_C2 and $P_3 = 0.091 \pm 0.009 \text{ cpp}$ in IP_C3. Interestingly, the modulation period in IP_C2 and IP_C3 is roughly twice that of MP_C2 and MP_C3, although the physical mechanism responsible for this relationship remains unclear. Periodic amplitude modulation has been reported in a number of MSPs (Wang et al. 2024). By contrast, subpulse drifting has been detected in only a few MSPs, and it is interesting to note that all of these cases occur in recycled systems, where the drifting is consistently weak and classified as diffuse rather than coherent (e.g., Edwards & Stappers 2003; Liu et al. 2016; Miao et al. 2023). In addition, since interpulse emission in MSPs is generally very weak, only one MSP, PSR J1012+5307, had previously shown evidence of periodic modulation in its interpulse emission (Wang et al. 2024). PSR J1857+0943 therefore becomes the second known MSP in which periodic modulation is detected in the interpulse region. These markedly different modulation behaviors among different profile components in PSR J1857+0943 demonstrate that their undergo distinct fluctuation processes.

The LRCCF further confirms the drifting and periodic modulation features revealed by the 2DFS. Notably, the nearly vertical ridge in MP_C3 indicates that this component does not undergo systematic phase drift but instead likely contains two preferred emission sites that alternate in intensity from pulse to pulse. Even more striking is the clear anticorrelation between MP_C3 and the interpulse components IP_C1 and IP_C2. Such an anticorrelation implies a physical linkage between MP_C3 and the interpulse, operating on timescales much longer than the rotation period. This finding suggests that, although MP_C2 and MP_C3 appear adjacent in the average profile, they may not originate from the same magnetic pole. Instead, MP_C3 is more naturally associated with the same pole as the interpulse.

Dyks (2017) shows that coherent mode addition and propagation can produce broad, loop- or V-shaped PPA bifurcations that are accompanied by enhanced $|V|$ and lowered L/I at the transition longitudes. For PSR J1857+0943, its single-pulse PPA distribution near pulse longitudes of 280° and 310° are compact and localized rather than broad or looped, they are not accompanied by strong $|V|$ peaks or L/I minima, and they occur together with component-specific fluctuation behaviour (drift in MP_C2, amplitude modulation in MP_C3 and

IP). These differences make the coherent mode addition explanation unlikely as the primary cause. Instead, the tight LRCCF anticorrelation between MP_C3 and the interpulse on long timescales, the similar modulation behaviour, and the matched, non-coherent mode addition PPA clusters together favor the interpretation that MP_C3 and the interpulse arise from the same magnetic pole or closely linked emission region.

Pulse jitter is expected to become a dominant source of timing uncertainty for millisecond pulsars as observing sensitivities continue to improve, making it essential to understand how jitter relates to pulse-profile properties. Population studies have established that pulse jitter is closely linked to the global properties of pulsar emission. Using large samples of millisecond pulsars, Lam et al. (2019) and Parthasarathy et al. (2021) reported a moderate correlation between rms jitter and the W_{50} , while finding no significant dependence on the W_{eff} . In this work, we investigate these relationships for PSR J1857+0943 at different frequency. We observe pronounced frequency evolution in both W_{50} and W_{eff} , consistent with systematic changes in the emission beam geometry and profile sharpness with observing frequency. However, despite this clear width evolution, the $\sigma_{J,1h}$, shows no statistically significant correlation with either W_{50} or W_{eff} . This apparent discrepancy with population-level trends can be understood if, for PSR J1857+0943, the observed jitter is dominated by the intrinsic stochasticity of the dominant emission component, whose single-pulse phase and amplitude statistics remain approximately invariant with frequency. In this

scenario, the frequency evolution of the integrated pulse width is primarily driven by changes in the visibility or relative contribution of weaker outer components, or by frequency-dependent propagation effects, rather than by variations in the underlying stochastic emission process that governs jitter.

1 This work was supported by the Strategic Priority
 2 Research Program of the Chinese Academy of Sciences,
 3 Grant No.XDA0350501, the Major Science and Technology Program of Xinjiang Uygur Autonomous Region (No.2022A03013-4), the Guizhou Provincial Basic Research Program (Natural Science) (No. Qiankehejichu-MS(2025)263), the Guizhou Provincial Science and Technology Projects (Nos. QKHFQ[2023]003, QKHPTRC-ZDSYS[2023]003, QKHFQ[2024]001-1), Guizhou Provincial Scientific and Technological Program The Postdoctoral Research Station of the Guizhou Radio Astronomical Observatory. (No.QKHPTRC[2021]Postdoctoral Research Station-001), the National Natural Science Foundation of China (No. 12041304), the Project funded by China Postdoctoral Science Foundation(No. 2023M743517). This work made use of the data from the Five-hundred-meter Aperture Spherical Radio telescope, which is a Chinese national mega-science facility, operated by the National Astronomical Observatories, Chinese Academy of Sciences.

REFERENCES

Agazie, G., Alam, M. F., Anumarlapudi, A., et al. 2023, ApJL, 951, L9, doi: [10.3847/2041-8213/acda9a](https://doi.org/10.3847/2041-8213/acda9a)

Backer, D. C. 1970, Nature, 228, 1297, doi: [10.1038/2281297a0](https://doi.org/10.1038/2281297a0)

Basu, R., Mitra, D., & Melikidze, G. I. 2020, ApJ, 889, 133, doi: [10.3847/1538-4357/ab63c9](https://doi.org/10.3847/1538-4357/ab63c9)

—. 2025, ApJ, 992, 105, doi: [10.3847/1538-4357/ae03c1](https://doi.org/10.3847/1538-4357/ae03c1)

Basu, R., Mitra, D., Melikidze, G. I., & Skrzypczak, A. 2019, MNRAS, 482, 3757, doi: [10.1093/mnras/sty2846](https://doi.org/10.1093/mnras/sty2846)

Chalumeau, A., Babak, S., Petiteau, A., et al. 2022, MNRAS, 509, 5538, doi: [10.1093/mnras/stab3283](https://doi.org/10.1093/mnras/stab3283)

Coles, W. A., Kerr, M., Shannon, R. M., et al. 2015, ApJ, 808, 113, doi: [10.1088/0004-637X/808/2/113](https://doi.org/10.1088/0004-637X/808/2/113)

Cordes, J. M., & Shannon, R. M. 2010, arXiv e-prints, arXiv:1010.3785, doi: [10.48550/arXiv.1010.3785](https://doi.org/10.48550/arXiv.1010.3785)

Deng, Z.-L., Gao, Z.-F., Li, X.-D., & Shao, Y. 2020, ApJ, 892, 4, doi: [10.3847/1538-4357/ab76c4](https://doi.org/10.3847/1538-4357/ab76c4)

Downs, G. S., & Reichley, P. E. 1983, ApJS, 53, 169, doi: [10.1086/190890](https://doi.org/10.1086/190890)

Drake, F. D., & Craft, H. D. 1968, Nature, 220, 231, doi: [10.1038/220231a0](https://doi.org/10.1038/220231a0)

Dyks, J. 2017, MNRAS, 472, 4598, doi: [10.1093/mnras/stx2101](https://doi.org/10.1093/mnras/stx2101)

Edwards, R. T., & Stappers, B. W. 2002, A&A, 393, 733, doi: [10.1051/0004-6361:20021067](https://doi.org/10.1051/0004-6361:20021067)

—. 2003, A&A, 407, 273, doi: [10.1051/0004-6361:20030716](https://doi.org/10.1051/0004-6361:20030716)

EPTA Collaboration, Antoniadis, J., Babak, S., et al. 2023, A&A, 678, A48, doi: [10.1051/0004-6361/202346841](https://doi.org/10.1051/0004-6361/202346841)

Han, J. L., Manchester, R. N., van Straten, W., & Demorest, P. 2018, ApJS, 234, 11, doi: [10.3847/1538-4365/aa9c45](https://doi.org/10.3847/1538-4365/aa9c45)

Hobbs, G. 2013, Classical and Quantum Gravity, 30, 224007, doi: [10.1088/0264-9381/30/22/224007](https://doi.org/10.1088/0264-9381/30/22/224007)

Hotan, A. W., van Straten, W., & Manchester, R. N. 2004, *pasa*, 21, 302, doi: [10.1071/AS04022](https://doi.org/10.1071/AS04022)

Jiang, P., Yue, Y., Gan, H., et al. 2019, *Science China Physics, Mechanics, and Astronomy*, 62, 959502, doi: [10.1007/s11433-018-9376-1](https://doi.org/10.1007/s11433-018-9376-1)

Jiang, P., Tang, N.-Y., Hou, L.-G., et al. 2020, *Research in Astronomy and Astrophysics*, 20, 064, doi: [10.1088/1674-4527/20/5/64](https://doi.org/10.1088/1674-4527/20/5/64)

Kerr, M., Reardon, D. J., Hobbs, G., et al. 2020, *PASA*, 37, e020, doi: [10.1017/pasa.2020.11](https://doi.org/10.1017/pasa.2020.11)

Kuzmin, A. D. 2007, *Ap&SS*, 308, 563, doi: [10.1007/s10509-007-9347-5](https://doi.org/10.1007/s10509-007-9347-5)

Lam, M. T., McLaughlin, M. A., Arzoumanian, Z., et al. 2019, *ApJ*, 872, 193, doi: [10.3847/1538-4357/ab01cd](https://doi.org/10.3847/1538-4357/ab01cd)

Li, D., Wang, P., Qian, L., et al. 2018, *IEEE Microwave Magazine*, 19, 112, doi: [10.1109/MMM.2018.2802178](https://doi.org/10.1109/MMM.2018.2802178)

Liu, K., Keane, E. F., Lee, K. J., et al. 2012, *MNRAS*, 420, 361, doi: [10.1111/j.1365-2966.2011.20041.x](https://doi.org/10.1111/j.1365-2966.2011.20041.x)

Liu, K., Bassa, C. G., Janssen, G. H., et al. 2016, *MNRAS*, 463, 3239, doi: [10.1093/mnras/stw2223](https://doi.org/10.1093/mnras/stw2223)

Liu, Y., Main, R. A., Verbiest, J. P. W., et al. 2023, *Science China Physics, Mechanics, and Astronomy*, 66, 119512, doi: [10.1007/s11433-023-2182-6](https://doi.org/10.1007/s11433-023-2182-6)

Mahajan, N., van Kerkwijk, M. H., Main, R., & Pen, U.-L. 2018, *ApJL*, 867, L2, doi: [10.3847/2041-8213/aae713](https://doi.org/10.3847/2041-8213/aae713)

Manchester, R. N., Hobbs, G. B., Teoh, A., & Hobbs, M. 2005, *aj*, 129, 1993, doi: [10.1086/428488](https://doi.org/10.1086/428488)

Miao, X. L., Zhu, W. W., Kramer, M., et al. 2023, *MNRAS*, 526, 2156, doi: [10.1093/mnras/stad2595](https://doi.org/10.1093/mnras/stad2595)

Miles, M. T., Shannon, R. M., Bailes, M., et al. 2022, *MNRAS*, 510, 5908, doi: [10.1093/mnras/stab3549](https://doi.org/10.1093/mnras/stab3549)

Nan, R., Li, D., Jin, C., et al. 2011, *International Journal of Modern Physics D*, 20, 989, doi: [10.1142/S0218271811019335](https://doi.org/10.1142/S0218271811019335)

Osłowski, S., van Straten, W., Hobbs, G. B., Bailes, M., & Demorest, P. 2011, *MNRAS*, 418, 1258, doi: [10.1111/j.1365-2966.2011.19578.x](https://doi.org/10.1111/j.1365-2966.2011.19578.x)

Özel, F., & Freire, P. 2016, *ARA&A*, 54, 401, doi: [10.1146/annurev-astro-081915-023322](https://doi.org/10.1146/annurev-astro-081915-023322)

Palliyaguru, N. T., Perera, B. B. P., McLaughlin, M. A., Osłowski, S., & Siebert, G. L. 2023, *MNRAS*, 520, 2747, doi: [10.1093/mnras/stad194](https://doi.org/10.1093/mnras/stad194)

Parthasarathy, A., Bailes, M., Shannon, R. M., et al. 2021, *MNRAS*, 502, 407, doi: [10.1093/mnras/stab037](https://doi.org/10.1093/mnras/stab037)

Ransom, S. M., Stairs, I. H., Archibald, A. M., et al. 2014, *Nature*, 505, 520, doi: [10.1038/nature12917](https://doi.org/10.1038/nature12917)

Segelstein, D. J., Rawley, L. A., Stinebring, D. R., Fruchter, A. S., & Taylor, J. H. 1986, *Nature*, 322, 714, doi: [10.1038/322714a0](https://doi.org/10.1038/322714a0)

Shannon, R. M., Osłowski, S., Dai, S., et al. 2014, *MNRAS*, 443, 1463, doi: [10.1093/mnras/stu1213](https://doi.org/10.1093/mnras/stu1213)

Song, X., Weltevrede, P., Szary, A., et al. 2023, *MNRAS*, 520, 4562, doi: [10.1093/mnras/stad135](https://doi.org/10.1093/mnras/stad135)

Sotomayor-Beltran, C., Sobey, C., Hessels, J. W. T., et al. 2013, *A&A*, 552, A58, doi: [10.1051/0004-6361/201220728](https://doi.org/10.1051/0004-6361/201220728)

Taylor, J. H. 1992, *Philosophical Transactions of the Royal Society of London Series A*, 341, 117, doi: [10.1098/rsta.1992.0088](https://doi.org/10.1098/rsta.1992.0088)

van Kerkwijk, M. H., Bell, J. F., Kaspi, V. M., & Kulkarni, S. R. 2000, *ApJL*, 530, L37, doi: [10.1086/312478](https://doi.org/10.1086/312478)

van Straten, W., & Bailes, M. 2011, *pasa*, 28, 1, doi: [10.1071/AS10021](https://doi.org/10.1071/AS10021)

Wang, S. Q., Hobbs, G., Wang, J. B., et al. 2020, *ApJL*, 902, L13, doi: [10.3847/2041-8213/abbb89](https://doi.org/10.3847/2041-8213/abbb89)

Wang, S. Q., Wang, J. B., Wang, N., et al. 2021, *ApJ*, 913, 67, doi: [10.3847/1538-4357/abf937](https://doi.org/10.3847/1538-4357/abf937)

Wang, S. Q., Wang, N., Wang, J. B., et al. 2024, *ApJ*, 964, 6, doi: [10.3847/1538-4357/ad217b](https://doi.org/10.3847/1538-4357/ad217b)

Wu, Q. D., Wang, N., Yuan, J. P., et al. 2023, *ApJL*, 958, L17, doi: [10.3847/2041-8213/ad0887](https://doi.org/10.3847/2041-8213/ad0887)

Xu, H., Chen, S., Guo, Y., et al. 2023, *Research in Astronomy and Astrophysics*, 23, 075024, doi: [10.1088/1674-4527/acdfa5](https://doi.org/10.1088/1674-4527/acdfa5)

Xu, J., Jiang, J., Xu, H., et al. 2025a, *A&A*, 695, A173, doi: [10.1051/0004-6361/202452960](https://doi.org/10.1051/0004-6361/202452960)

Xu, X., Zhi, Q., Bai, J., et al. 2024, *ApJ*, 968, 119, doi: [10.3847/1538-4357/ad4889](https://doi.org/10.3847/1538-4357/ad4889)

Xu, X., Dai, S., Zhi, Q., et al. 2025b, *ApJ*, 982, 117, doi: [10.3847/1538-4357/adbb65](https://doi.org/10.3847/1538-4357/adbb65)

Zhang, D., Tao, Z., Yuan, M., et al. 2023, *Science China Physics, Mechanics, and Astronomy*, 66, 299511, doi: [10.1007/s11433-023-2138-5](https://doi.org/10.1007/s11433-023-2138-5)

Zhu, W. W., Stairs, I. H., Demorest, P. B., et al. 2015, *ApJ*, 809, 41, doi: [10.1088/0004-637X/809/1/41](https://doi.org/10.1088/0004-637X/809/1/41)

APPENDIX

A. DERIVATION OF THE MODULATION INDEX

In the case of using a single off-pulse window, we first consider the statistical properties of the off-pulse region. Let N denote the number of phase points in the off-pulse region, where each point follows a normal distribution with mean μ_0 and standard deviation σ_0 . During the baseline removal process, the mean of the off-pulse region is calculated for each pulse, and the baseline is subtracted. This mean follows a normal distribution with mean μ_0 and standard deviation $\frac{\sigma_0}{\sqrt{N}}$.

After baseline removal, the off-pulse mean becomes zero, and its standard deviation is reduced to

$$\sigma_1 = \sqrt{\frac{N-1}{N}}\sigma_0 \quad (\text{A1})$$

For the on-pulse region, the observed standard deviation σ_{on} and mean μ_{on} relate to the intrinsic pulse properties through

$$\sigma_{\text{on}} = \sqrt{\sigma_{\text{pulse}}^2 + \frac{N+1}{N}\sigma_0^2}, \quad \mu_{\text{on}} = \mu_{\text{pulse}}, \quad (\text{A2})$$

where σ_{pulse} and μ_{pulse} are the true standard deviation and mean of the pulse emission. Substituting the expressions for the baseline variance, we obtain

$$\sigma_{\text{pulse}} = \sqrt{\sigma_{\text{on}}^2 - \frac{N+1}{N-1}\sigma_1^2}, \quad (\text{A3})$$

and thus, the corrected modulation index is

$$m = \frac{\sigma_{\text{pulse}}}{\mu_{\text{on}}} = \frac{\sqrt{\sigma_{\text{on}}^2 - \frac{N+1}{N-1}\sigma_1^2}}{\mu_{\text{on}}}. \quad (\text{A4})$$

The above derivation indicates that baseline subtraction introduces a systematic effect on the estimation of the modulation index. When the standard deviation of the off-pulse region, denoted as σ_1 , is used as the reference noise level, the pulse-phase variance σ_{pulse}^2 is effectively overestimated by $\frac{2}{N}\sigma_0^2$. For most pulsars, σ_0 is typically comparable to or even larger than σ_{pulse} , leading to an overestimation of the modulation index, especially in pulse-phase bins near the profile edges where the mean intensity is relatively low. To preserve the variance characteristics of different phase bins after baseline removal, the corresponding regions should be multiplied by a correction factor of $\frac{N+1}{N-1}$. This adjustment ensures that the variance properties remain consistent across all pulse-phase bins. Moreover, the baseline subtraction process itself reduces the single-pulse signal-to-noise ratio along the pulse sequence by a factor of $\frac{N+1}{N}$. Therefore, the baseline should ideally be estimated using as many phase bins as possible to minimize this effect. Since the radiation intensity is intrinsically non-negative, a modulation index significantly larger than 2 implies that the instantaneous intensity fluctuates well above the mean level. Such large fluctuations suggest that the emission at that particular phase longitude may be dominated by sporadic giant pulses.